


# Characteristic analysis of scattering field in two-layer media by Green's function

Ping Zhang(张萍), Zhi-Ying Liu(刘智颖), Shou-Guo Yan(阎守国), Juan Huang(黄娟), and Bi-Xing Zhang(张碧星)
**Citation:**Chin. Phys. B, 2023, 32 (**6**): 064301. DOI: 10.1088/1674-1056/aca3a0
Journal homepage: http://cpb.iphy.ac.cn; http://iopscience.iop.org/cpb

**What follows is a list of articles you may be interested in**

---

## Reconfigurable source illusion device for airborne sound using an enclosed adjustable piezoelectric metasurface

Yi-Fan Tang(唐一璠) and Shu-Yu Lin(林书玉)
Chin. Phys. B, 2023, 32 (**3**): 034306. DOI: 10.1088/1674-1056/ac9fc0

## Response characteristics of drill-string guided wave in downhole acoustic telemetry

Ao-Song Zhao(赵傲耸), Hao Chen(陈浩), Xiao He(何晓), Xiu-Ming Wang(王秀明), and Xue-Shen Cao(曹雪砷)
Chin. Phys. B, 2023, 32 (**3**): 034301. DOI: 10.1088/1674-1056/ac8e98

## Effect of porous surface layer on wave propagation in elastic cylinder immersed in fluid

Na-Na Su(苏娜娜), Qing-Bang Han(韩庆邦), Ming-Lei Shan(单鸣雷), and Cheng Yin(殷澄)
Chin. Phys. B, 2023, 32 (**1**): 014301. DOI: 10.1088/1674-1056/ac6ee6

## Quantitative damage imaging using Lamb wave diffraction tomography

Hai-Yan Zhang(张海燕), Min Ruan(阮敏), Wen-Fa Zhu(朱文发), Xiao-Dong Chai(柴晓冬)
Chin. Phys. B, 2016, 25 (**12**): 124304. DOI: 10.1088/1674-1056/25/12/124304

## Seismoelectric waves in a borehole excited by an external explosive source

Zhou Jiu-Guang (周久光), Cui Zhi-Wen (崔志文), Lü Wei-Guo (吕伟国), Zhang Yu-Jun (张玉君), Wang Ke-Xie (王克协)
Chin. Phys. B, 2014, 23 (**1**): 014301. DOI: 10.1088/1674-1056/23/1/014301

---

# Characteristic analysis of scattering field in two-layer media by Green's function

Ping Zhang(张萍)[1,2,†], Zhi-Ying Liu(刘智颖)[1,3,†], Shou-Guo Yan(阎守国)[1,‡], Juan Huang(黄娟)[1], and Bi-Xing Zhang(张碧星)[1,3]

[1] *Key Laboratory of Acoustics, Institute of Acoustics, Chinese Academy of Sciences, Beijing* 100190, *China*
[2] *Key Laboratory of Nondestructive Testing, Ministry of Education, Nanchang Hangkong University, Nanchang* 330063, *China*
[3] *University of Chinese Academy of Sciences, Beijing* 100190, *China*

(Received 22 September 2022; revised manuscript received 9 November 2022; accepted manuscript online 17 November 2022)

The problem of three-dimensional (3D) acoustic scattering in a complex medium has aroused considerable interest of researchers for many years. An ultrasonic scattered field calculating technique is proposed to study the scattering echo from strongly scattered materials in a two-layer medium in this work. Firstly, with the high frequency stationary phase method, the Green's function of two-layer fluid media is derived. And then based on the idea of integral equation discretization, the Green's function method is extended to two-layer fluid media to derive the scattering field expression of defects in a complex medium. With this method, the scattering field of 3D defect in a two-layer medium is calculated and the characteristics of received echoes are studied. The results show that this method is able to solve the scattering P wave field of 3D defect with arbitrary shape at any scattering intensity in two-layer media. Considering the circumstance of water-immersion ultrasonic non-destructive test (NDT), the scattering sound field characteristics of different types of defects are analyzed by simulation, which will help to optimize the detection scheme and corresponding imaging method in practice so as to improve the detection quality.

**Keywords:** Green's function method, two-layer media, scattering field, water-immersed detection

**PACS:** 43.20.+g, 43.35.+d, 43.90.+v **DOI:** 10.1088/1674-1056/aca3a0

## 1. Introduction

The accurate calculation of scattered sound field is very important in producing the map of the acoustical properties of a region of interest (ROI). This map is very useful in nondestructive testing,[1,2] geophysics[3] or medical diagnosis.[4,5] In many practical cases, the region of interest is not composed of homogeneous media but of layered media. It is of great interest to improve the calculating capability of layered model to obtain more information about the inspected region. So far, to our knowledge, many researches have been done on acoustic field calculation in layered media by using angular spectrum method,[6,7] multi-Gaussian beam (MGB) model,[8] or distributed point source method.[9,10] With regard to the calculation of scattered sound field from scatterer in layered media, there is no analytical expression due to the influence of boundary conditions.

In the field of medical ultrasound, the difference in acoustic impedance between the scatterer and the tissue is not very great. So, generally, the Born approximation or some other perturbation approximation methods are considered to primarily simulate the scattering acoustic field.[11] However, in the field of industrial ultrasonic nondestructive testing, the difference in acoustic impedance between the scatterer (defect) and the medium is usually quite great. In this strongly scattering case, high contrast causes the total field inside the scatterer to be too different from the incident field, thus the Born assumption is no longer applicable.[12] Darmon *et al.*[13] and Huang *et al.*[14] presented and modified the doubly distorted Born approximation to handle this problem so as to achieve the response of both strong and weak scattering inclusions. However, the modified Born approximation fails to simulate the scattering field in layered media because it is an analytical solution and incapable of dealing with layered issues.

Chen and Zheng[15] concerned the numerical solution of the acoustic scattering problems in a two-dimensional (2D) two-layer medium, and introduced an uniaxial finite element perfectly matched layer (PML) method to solve the radiation conditions. Jiang and Yuan[16] developed an adaptive finite element PML method and investigated its exponential convergence. Although these purely numerical methods can be very effective in such complicated cases, it is generally harder to implement in 3D problem, because its calculation is large and takes a long time. In addition, the results of finite element method consist of both the interface echo and scattering echo caused by objects, which cannot be separated and analyzed individually.

In order to reduce the computing time, several authors have adopted semi-analysis methods. Zampolli *et al.*[17] computed the far field radiated by 3D objects inside layered fluid

[†]These authors contributed equally to this work.
[‡]Corresponding author. E-mail: yanshouguo@mail.ioa.ac.cn

© 2023 Chinese Physical Society and IOP Publishing Ltd 

media by using the approximate Green's function to reduce the computing time, while this method requires the pressure and normal particle displacement on the surface of the object as an input. Boag *et al.*[18] presented a moment method solution for the 3D problem of acoustic scattering from homogeneous fluid bodies. The basic idea[19] of this numerical method is to transform a functional equation into a matrix equation, and then solve the matrix equation by inversion or elimination, and thus avoiding carrying out numerical integrations. Combining this idea with the sound wave equation and the Green's function, the sound fields inside and outside the scatterer can be computed straightforwardly and precisely. Obviously, it is feasible to extend the above method from infinite uniform medium to a two-layer medium, and the core is the Green's function in a layered medium. With this method, the exact 3D scattering field of object in a two-layer medium can be fast-obtained and high-accuracy.

This work focuses on calculating and analyzing the exact scattering echo and 3D scattering field distribution from defects in a two-layer medium, which is desirable to improve simulation performance and study the sound scattering behavior of different defects in water-immersed detection. First, with the method of stationary phase at high frequency, the analytical expression of Green's function in two-layer fluid media is derived, which can be used to calculate the sound field in layered media. And then, Green's function method (GFM) is extended from infinite uniform medium to two-layer media for calculating the precise scattering sound field. The accuracy of this proposed method is verified by comparing the results calculated by the proposed method with those from the finite element method. Additionally, the advantages and shortcomings are discussed. Finally, we analyze the scattering fields of different defects in a water-immersed steel medium such as spherical hole, flat-bottom hole, through-hole, and crack defect, which provides technical guidance for water-immersed detection.

## 2. Green's function in two-layer media

If there is a fluid–fluid interface, and $\rho_1 c_1$, $\rho_2$ $c_2$ are the density and sound speed of the first and second layer mediums respectively as shown in Fig. 1, let sound source point be located at $\boldsymbol{r}' = (x', y', z')$ in the first layer, and plane $z = 0$ be the interface between two layers, perpendicular to the $z$ axis. A second cylindrical coordinate system is defined at $O'$, which is the projection of point $\boldsymbol{r}'$ onto plane $z = 0$. Therefore, the sound field at point $\boldsymbol{r} = (x, y, z)$ is symmetric about the new $z$ axis, which means that the coordinate $\theta$ has no influence on the result of sound field. Then, we make $\boldsymbol{r}' = (0, z'), \boldsymbol{r} = (r, z)$, where $r = \sqrt{(x-x')^2 + (y-y')^2}$.

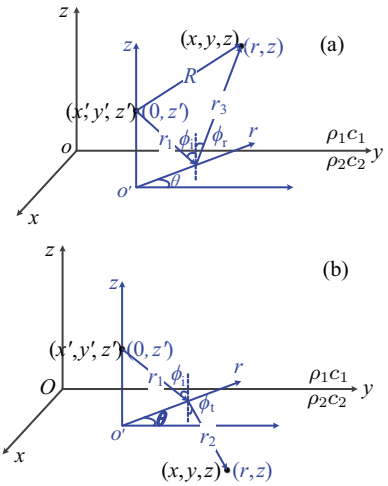



**Fig. 1.** Schematic diagram showing geometric relationship when solving Green's function of a two-layer fluid medium, with if field point located in (a) the first layer and (b) the second layer.

It can be seen from Fig. 1 that the Green's function of the first layer can be obtained by superposing the incident and reflected sound fields generated by the point source, and that of the second layer is obtained by the sound field refracted from the point source through the interface.

According to Green's function in an infinite homogeneous medium

$$G(\boldsymbol{r}, \boldsymbol{r}') = \frac{\mathrm{e}^{\mathrm{i}k|\boldsymbol{r}-\boldsymbol{r}'|}}{4\pi|\boldsymbol{r}-\boldsymbol{r}'|}, \tag{1}$$

and boundary conditions at fluid–fluid interface, using the method of stationary phase[20] under high frequency, the relationship among incident angle, reflection angle, and refraction angle can be deduced as follows:

$$\begin{cases} \phi_\mathrm{i} = \phi_\mathrm{r}, \\ k_1 \sin\phi_\mathrm{i} = k_2 \sin\phi_\mathrm{t}, \end{cases} \tag{2}$$

and then the Green's function of two-layer fluid media can be obtained

$$G(\boldsymbol{r}, \boldsymbol{r}') = \begin{cases} \frac{\mathrm{e}^{\mathrm{i}k_1 R}}{4\pi R} + R(\phi_\mathrm{i}) \frac{\mathrm{e}^{\mathrm{i}k_1(r_1+r_3)}}{4\pi(r_1+r_3)}, & z \geq 0, \\ T(\phi_\mathrm{i}) \frac{\mathrm{e}^{\mathrm{i}(k_1 r_1 + k_2 r_2)}}{4\pi\sqrt{(r_1+n'r_2)(r_1+n'r_2\cos^2\phi_\mathrm{i}/\cos^2\phi_\mathrm{t})}}, & z < 0, \end{cases} \tag{3}$$

where $n' = c_2/c_1$,

$$R(\phi_\mathrm{i}) = \frac{\rho_2 c_2 \cos\phi_\mathrm{i} - \rho_1 c_1 \cos\phi_\mathrm{t}}{\rho_2 c_2 \cos\phi_\mathrm{i} + \rho_1 c_1 \cos\phi_\mathrm{t}},$$

$$T(\phi_\mathrm{i}) = \frac{2\rho_2 c_2 \cos\phi_\mathrm{i}}{\rho_2 c_2 \cos\phi_\mathrm{i} + \rho_1 c_1 \cos\phi_\mathrm{t}},$$

where $\phi_\mathrm{i}$ and $\phi_\mathrm{t}$ are the angles of incidence and refraction respectively, and the relationship among $r_1$, $r_2$, and $r_3$ is shown in Fig. 1.

It should be noted that the derived Green's function is capable of representing the bulk waves radiating inside the medium, which neglects the lateral waves transmitting along the interface in far field.

## 3. Green's function method to calculate scattering echo from scatterer in fluid–fluid media

As shown in Fig. 2, there is an inhomogeneous arbitrarily shaped scatterer located at $\boldsymbol{r}_{\rm sct}$ in the second layer fluid medium, and its volume is written as $V$, illuminated by point source from $\boldsymbol{r}_{\rm s}$ in the first layer. The interface between the two fluid media is in the *xoy* plane. And the excitation signal of the point source is $F(\omega)$.

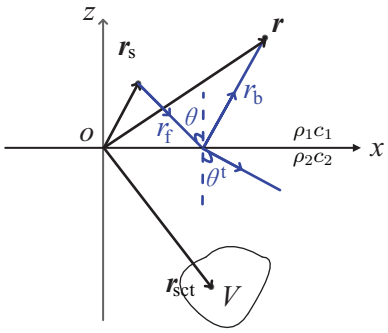



**Fig. 2.** Schematic diagram of interface echo calculation in a two-layer fluid medium.

Given that the sound source point and the receiver transducer are located in the first layer and the scatterer is inside the region $V$ in the second layer, the problem is how to calculate the echo signal received by the transducer when the source point emits sound wave. Apparently, the received signal of the transducer can be described as the summation of three parts: direct wave, interface echo and scattering echo.

### 3.1. Direct wave and interface echo

The transmit paths of the interface echo from source point $O$ to the receive point $\boldsymbol{r}$ are $r_{\rm f}$, and $r_{\rm b}$ as shown in Fig. 2, and the values of $\theta$, $\theta^{\rm t}$, $r_{\rm f}$, $r_{\rm b}$ could be deduced according to the relationship between $\boldsymbol{r}_{\rm s}$ and $\boldsymbol{r}$ and Eq. (2). Thus, the received direct wave and interface echo can be written as

$$P_{\rm inter} = F(\omega)\cdot\left(\frac{{\rm e}^{{\rm i}k_1|\boldsymbol{r}_{\rm re}|}}{4\pi|\boldsymbol{r}_{\rm re}|}+\frac{\rho_2c_2\cos\theta-\rho_1c_1\cos\theta^{\rm t}}{\rho_2c_2\cos\theta+\rho_1c_1\cos\theta^{\rm t}}\cdot\frac{{\rm e}^{{\rm i}k_1(r_{\rm f}+r_{\rm b})}}{4\pi(r_{\rm f}+r_{\rm b})}\right), \quad (4)$$

where $\boldsymbol{r}_{\rm re}=\boldsymbol{r}-\boldsymbol{r}_{\rm s}$.

### 3.2. Scattering echo

In some strongly scattering cases, the Born assumption is no longer applicable to calculating the scattering echo. Aiming at this problem, the GFM is proposed to deduce the accurate solution of the scattering field.

Without considering the interface echo, we directly calculate the scattering echo received by the transducer in two-layer media in this subsection. Suppose that the sound speed inside the scatter is $c_{\rm sct}$ and wave number is $k_{\rm sct}=\omega/c_{\rm sct}$, both of which are a function of coordinate $\boldsymbol{r}_{\rm sct}$. The wavenumber of the layered media is written as $k$, $k=\omega/c$, where $c$ equals $c_1$ in the first layer medium, and $c_2$ in the second layer medium. Thus the acoustic pressure $P$ inside and outside the scatterer is governed by the following equation:

$$\begin{cases}\left(\nabla^2+k_{\rm sct}^2\right)P=0, & \boldsymbol{r}\in V,\\ \left(\nabla^2+k^2\right)P=0, & \boldsymbol{r}\notin V.\end{cases} \quad (5)$$

Now, we come to define an inhomogeneous coefficient $S$ to characterize the internal properties of the scatterer, and $S$ equals 0 outside the scatter, such that

$$S=\begin{cases}1-\dfrac{k_{\rm sct}^2}{k^2}=1-\dfrac{c^2}{c_{\rm sct}^2}, & \boldsymbol{r}\in V,\\ 0, & \boldsymbol{r}\notin V.\end{cases} \quad (6)$$

Then equation (5) can be written as

$$\left(\nabla^2+k^2\right)P=k^2SP, \quad (7)$$

where $P$ is the sum of incident and scattered sound fields, *i.e.*,

$$P=P_{\rm i}+P_{\rm s}, \quad (8)$$

with $P_{\rm i}$ denoting the incident sound field, thus there exits $\left(\nabla^2+k^2\right)P_{\rm i}=0$, and equation (7) changes into the following form:

$$\left(\nabla^2+k^2\right)P_{\rm s}=k^2SP. \quad (9)$$

Combining the above equation and the Green's function, the solution of the scattered sound field can be obtained to be

$$P_{\rm s}(\boldsymbol{r})=-k^2\int_V G(\boldsymbol{r},\boldsymbol{r}_{\rm sct})S(\boldsymbol{r}_{\rm sct})P(\boldsymbol{r}_{\rm sct})\,{\rm d}^3\boldsymbol{r}_{\rm sct}, \quad (10)$$

where $P(\boldsymbol{r}_{\rm sct})$ is the total field inside the scatterer $\boldsymbol{r}_{\rm sct}$, according to Eq. (8), $P(\boldsymbol{r})$ can be written as

$$P(\boldsymbol{r})=P_{\rm i}(\boldsymbol{r})-k^2\int_V G(\boldsymbol{r},\boldsymbol{r}_{\rm sct})S(\boldsymbol{r}_{\rm sct})P(\boldsymbol{r}_{\rm sct})\,{\rm d}^3\boldsymbol{r}_{\rm sct}. \quad (11)$$

With regard to a sound source with intensity $F$, the incident field $P_{\rm i}$ can be written as

$$P_{\rm i}(\boldsymbol{r})=FG(\boldsymbol{r},\boldsymbol{r}_{\rm s}), \quad (12)$$

where $G(\boldsymbol{r},\boldsymbol{r}_{\rm s})$ represents the Green's function at $\boldsymbol{r}$ inspired by source point $\boldsymbol{r}_{\rm s}$, and is given by Eq. (3).

There is sound pressure $P(\boldsymbol{r})$ both on the left and right sides of Eq. (11), which makes it difficult to calculate $P(\boldsymbol{r})$. In the Born approximation, the pressure $P(\boldsymbol{r})$ inside the integral sign is assumed to be the incident sound pressure $P_{\rm i}(\boldsymbol{r})$ in order to simplify the calculation. This perturbation approximation can be effective in the weak scattering model. Moreover, the Born approximation or some modified approximation methods[13] are limited to the frequency and the size of scatterer.

By using the method of moments,[21] the precise solution of strongly scattering problems can be obtained. As shown

in Fig. 3, the region inside the scatterer is discretized and divided into $M$ grids. During the discretization, the volume of the grid is small enough so that the scattering intensity in each small grid can be taken as a constant. Therefore, equation (11) could be discretized into

$$P_m = P_{\mathrm{i}m} - k^2 \sum_{m'=1}^{M} G(\boldsymbol{r}_m, r_{m'}) S_{m'} P_{m'} \Delta V_{m'}, \tag{13}$$

where $P_m$ is total sound field at the $m$-th grid of the region, $m = 1, 2, \ldots, M$, $\boldsymbol{r}_{m'}$ is the position coordinate of the $m'$-th grid, $S_{m'}$ and $\Delta V_{m'}$ are the scattering intensity and volume of the $m'$-th grid, respectively.

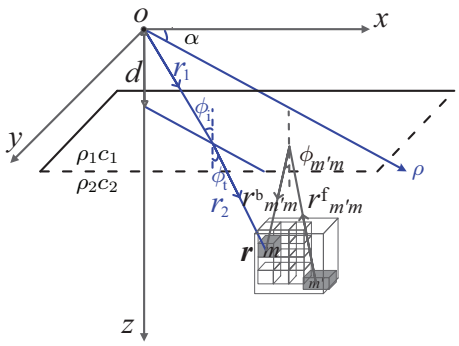



**Fig. 3.** The 3D model of GFM to calculate scattering echo.

In the case of the scattterer located in the second layer, the $G(\boldsymbol{r}_m, \boldsymbol{r}_{m'})$ is derived as follows:

$$G(\boldsymbol{r}_m, \boldsymbol{r}_{m'}) = \frac{\mathrm{e}^{\mathrm{i}k|\boldsymbol{r}_m - \boldsymbol{r}_{m'}|}}{4\pi|\boldsymbol{r}_m - \boldsymbol{r}_{m'}|} + R(\phi_{m'm}) \frac{\mathrm{e}^{\mathrm{i}k\left(r^{\mathrm{f}}_{m'm} + r^{\mathrm{b}}_{m'm}\right)}}{4\pi\left(r^{\mathrm{f}}_{m'm} + r^{\mathrm{b}}_{m'm}\right)}, \tag{14}$$

where $r^{\mathrm{f}}_{m'm}$ and $r^{\mathrm{b}}_{m'm}$ are the sound wave transmit path and incident path from point $\boldsymbol{r}_{m'}$ to point $\boldsymbol{r}_m$, and $\phi_{m'm}$ is the angle of incident as shown in Fig. 3. All values in Eq. (14) could be obtained according to Eq. (2). It should be noted that the value of $G(\boldsymbol{r}_m, \boldsymbol{r}_{m'})$ becomes divergent when $m = m'$. Now we make

$$g_{mm'} = k^2 G(\boldsymbol{r}_m, \boldsymbol{r}_{m'}) \Delta V_{m'}. \tag{15}$$

So if $m = m'$,

$$k^2 \int_{\Delta V} \frac{\mathrm{e}^{\mathrm{i}k|\boldsymbol{r}_m - \boldsymbol{r}'|}}{|\boldsymbol{r}_m - \boldsymbol{r}'|} \mathrm{d}^3\boldsymbol{r}' = (1 - \mathrm{i}ka)\,\mathrm{e}^{\mathrm{i}ka} - 1, \tag{16}$$

where $a$ is the radius of the $m$-th grid which satisfies $\Delta V_m = (4\pi/3)a^3$.

Therefore, the value of $g_{mm'}$ can be obtained to be

$$g_{mm'} = \begin{cases} k^2 \dfrac{\mathrm{e}^{\mathrm{i}k|\boldsymbol{r}_m - \boldsymbol{r}_{m'}|}}{4\pi|\boldsymbol{r}_m - \boldsymbol{r}_{m'}|} \Delta V_{m'} + k^2 \cdot \dfrac{\rho_1 c_1 \phi_{m'm} - \rho_2 c_2 \cos\phi^{\mathrm{t}}_{m'm}}{\rho_1 c_1 \phi_{m'm} + \rho_2 c_2 \cos\phi^{\mathrm{t}}_{m'm}} \cdot \dfrac{\mathrm{e}^{\mathrm{i}k\left(r^{\mathrm{f}}_{m'm} + r^{\mathrm{b}}_{m'm}\right)}}{4\pi\left(r^{\mathrm{f}}_{m'm} + r^{\mathrm{b}}_{m'm}\right)} \Delta V_{m'}, & m \neq m', \\ \mathrm{e}^{\mathrm{i}ka}(1 - \mathrm{i}ka) - 1 + k^2 \cdot \dfrac{\rho_1 c_1 - \rho_2 c_2}{\rho_1 c_1 + \rho_2 c_2} \cdot \dfrac{\mathrm{e}^{\mathrm{i}\cdot 2kr_{\mathrm{md}}}}{8\pi r_{\mathrm{md}}} \Delta V_{m'}, & m = m', \end{cases} \tag{17}$$

where $r_{\mathrm{md}}$ is the vertical distance between the interface and the center of the $m$-th grid.

So equation (13) can be written in the form of matrix

$$\boldsymbol{P} = \boldsymbol{P}_{\mathrm{i}} - \boldsymbol{Q}\boldsymbol{P}, \tag{18}$$

where

$$\boldsymbol{P} = (P_1, P_2, \ldots, P_m, \ldots, P_M)^{\mathrm{T}}, \tag{19}$$

$$\boldsymbol{P}_{\mathrm{i}} = (P_{\mathrm{i}1}, P_{\mathrm{i}2}, \ldots, P_{\mathrm{i}m}, \ldots, P_{\mathrm{i}M})^{\mathrm{T}}, \tag{20}$$

$$\boldsymbol{Q} = \begin{pmatrix} g_{11}S_1 & g_{12}S_2 & \cdots & g_{1M}S_M \\ g_{21}S_1 & g_{22}S_2 & \cdots & g_{2M}S_M \\ \vdots & \vdots & \ddots & \vdots \\ g_{M1}S_1 & g_{M2}S_2 & \cdots & g_{MM}S_M \end{pmatrix}. \tag{21}$$

$\boldsymbol{Q}$ is a square matrix, and means that the total field $\boldsymbol{P}$ inside the scatterer is given by

$$\boldsymbol{P} = (\boldsymbol{E} + \boldsymbol{Q})^{-1} \boldsymbol{P}_{\mathrm{i}}, \tag{22}$$

where $\boldsymbol{E}$ is a unit matrix. In this way, the integral equation (11) can be transformed into a matrix equation and solved by inversion, simplifying the calculation while ensuring the accuracy to the greatest extent.

Once we obtain the accurate solution of sound pressure $\boldsymbol{P}$ inside the scatterer, the scattering sound field of the receive point can be obtained. Discretizing equation (10) leads to the following expression of the scattering field at received point $\boldsymbol{r}$ in the first layer:

$$P_{\mathrm{s}}(\boldsymbol{r}) = -k^2 \sum_{m=1}^{M} G(\boldsymbol{r}, \boldsymbol{r}_m) S_m P_m \Delta V_m. \tag{23}$$

Supposing that there are $N$ receiving points located in the first layer, $G_{mn} = G(\boldsymbol{r}_n, \boldsymbol{r}_m)$ can be used to represent the Green's function at the $n$-th receiving point inspired by the $m$-th grid inside the scatterer. Thus the source point is at the second layer, and the receiving point is at the first layer. According to the reciprocal relationship[22] in sound field, the Green's function can be given by

$$G(\boldsymbol{r}_n, r_m) = \frac{\rho_1}{\rho_2} G(\boldsymbol{r}_m, r_n). \tag{24}$$

Here the source point $\boldsymbol{r}_m$ and the receiving point $\boldsymbol{r}_n$ are located in different media, so $G_{mn}$ is convergent. Defining the matrix concluding the Green's function such that $g_{mn} = k^2 G_{mn} \Delta V_m$ and $Q'_{mn} = g_{mn} S_m$, the scattered sound field at the receiving point $\boldsymbol{r}$ can be written as a matrix

$$\boldsymbol{P}_\mathrm{s} = \left(P_\mathrm{s}(\boldsymbol{r}_1), P_\mathrm{s}(\boldsymbol{r}_2), \ldots P_\mathrm{s}(\boldsymbol{r}_n), \ldots, P_\mathrm{s}(\boldsymbol{r}_N)\right)^\mathrm{T}, \tag{25}$$

and $Q'_{mn}$ in the form of matrix

$$\boldsymbol{Q}' = \begin{pmatrix} g_{11}S_1 & g_{12}S_2 & \cdots & g_{1N}S_M \\ g_{21}S_1 & g_{22}S_2 & \cdots & g_{2N}S_M \\ \vdots & \vdots & \ddots & \vdots \\ g_{M1}S_1 & g_{M2}S_2 & \cdots & g_{MN}S_M \end{pmatrix}. \tag{26}$$

Therefore, we can obtain the accurate scattering field in fluid–fluid model:

$$\boldsymbol{P}_\mathrm{s} = -\boldsymbol{Q}'\left(\boldsymbol{E} + \boldsymbol{Q}\right)^{-1} \boldsymbol{P}_\mathrm{i}. \tag{27}$$

## 4. Model validation

As mentioned before, a cosine envelope function modulated by Hanning window is chosen as an excitation source in an attempt to simulate the realistic scattering field, which can be written as

$$f_\mathrm{e}(t) = \begin{cases} \dfrac{1}{2}\left\{1 + \cos\left[\dfrac{2\pi}{t_\mathrm{c}}\left(t - \dfrac{t_\mathrm{c}}{2}\right)\right]\right\} \\ \times \cos\left[2\pi f_0\left(t - \dfrac{t_\mathrm{c}}{2}\right)\right] \cdot w(t), & 0 \le t \le t_\mathrm{c}, \\ 0, & t < 0, t > t_\mathrm{c}, \end{cases} \tag{28}$$

where $f_0$ is the center frequency, $t_\mathrm{c}$ is the pulse duration, and $w(t)$ is the Hanning window. In the simulation, the parameters are selected as $t_\mathrm{c} = 5/f_0$.

### 4.1. Scattering echo in fluid–fluid model

Considering the fluid–fluid case, we select gasoline and water as the first layer medium and the second layer medium, respectively, and their parameters are listed in Table 1. The source point is located in the first layer at point $O$. The horizontal distance between the source and the defect can be written as $R_x$ , which is supposed to be small in order to achieve a small incident angle to study the P wave propagation behavior, and here we make $R_x$ equal 0 firstly. The depth between the source point and the interface is set to 11 mm, and that between the source point and the scatterer is set to 16 mm, and parameters of the media are listed in Table 1. The radius of the scatterer is set to $0.22\lambda_\mathrm{water}$, which implies $ka = 1.4$. And the side length of the small discretized grid is set to 1/16 $\lambda_\mathrm{water}$, so the number of the small grids equals 203. According to these parameters, the spectrum of scattered echo signal $P_\mathrm{s}$ at any receiving point in the first layer can be obtained from Eq. (27).

**Table 1.** Parameters of fluid–fluid media.

| Medium | Material | Density (kg/m$^3$) | Velocity (m/s) | Depth (mm) |
|---|---|---|---|---|
| First layer medium | gasoline | 700 | 1250 | 11 |
| Second layer medium | water | 1000 | 1500 | – |
| Scatterer | steel | 7850 | 5778 | 16 |

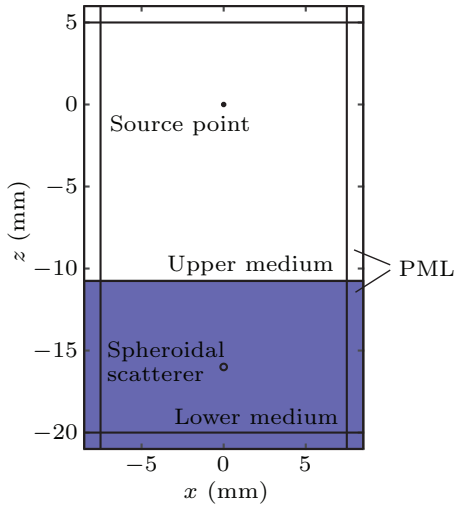



**Fig. 4.** The FEM simulation model for scattering field of defects in fluid–fluid media.

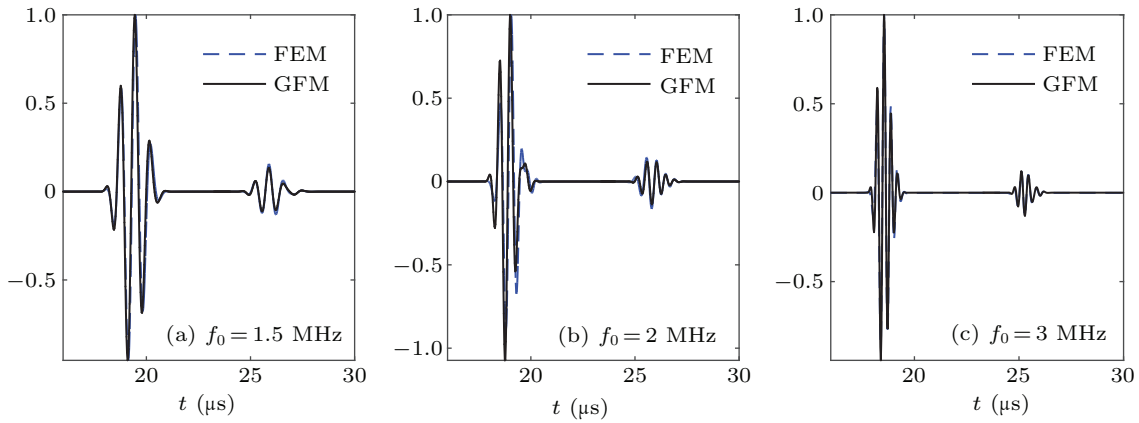



**Fig. 5.** Scattering echoes from steel sphere in the second layer of fluid–fluid model at different frequencies calculated by two methods: GFM (solid line) and finite element method (dashed line).

In order to verify the correctness of $P_s$, the scattering echo received at the source point is calculated by using the two methods: GFM and time-domain finite element method (FEM). The FEM model is shown in Fig. 4, in which a spherical scattering object is located in a two-layer fluid space and a source point is considered. The whole computation domain needs to be divided into the meshes each with a size smaller than $\lambda/5$, which makes transient calculation of the 3D model in this paper almost impossible. In order to simplify the calculation of FEM model, in this paper a simple 2D model is adopted, with the point source located just above the defect of the second layer. There is a layer of PML surrounding the computational domain that absorbs all the waves that propagate from the inside computational domain. The thickness of PML is 1 mm, and there are 12 layers of divided grid inside the PML.

Results in different values of center frequency $f_0$ are obtained, which are shown in Fig. 5. As shown in the figure, the normalized time-domain echo signal obtained by inverse Fourier transform of $P_s$ is the solid black line and the FEM result is plotted in blue dashed line. There are two wavelets in the received signal, where the first received signal is the interface echo and the second signal is the scattering echo. It can be observed that results from the two methods are in good agreement with each other, which demonstrates the correctness of GFM.

### 4.2. Scattering echo in fluid–solid model

The proposed GFM model is suitable for the calculation of defect echo of fluid–fluid model, where the field to be calculated is sound pressure of scattered P wave. While, in the ultrasonic nondestructive testing, a commonly encountered case is the defect echo in fluid–solid model. In the case of fluid–solid model, the sound wave becomes both P wave and S wave when they transmit into the solid medium. Generally, due to the smaller angle of incidence in practical test, the energy of S wave in the solid converted from the P wave in the fluid is less. Therefore, the S wave can be ignored in order to simplify the problem, we can ignore the S wave and mainly investigate the propagation behavior of P wave.[23] On this premise, the fluid–solid model can be regarded as a fluid–fluid model, where the GFM model can be used to calculate the P wave echo. The accuracy of the GFM result is evaluated bycomparing that of the reslus from the FEM model.

The FEM fluid–solid model considered is shown in Fig. 6, and the acoustic parameters of the media are listed in Table 2. The fluid medium is surrounded by a 0.75-mm-thick PML layer, and there are also 12 layers of grid inside the PML. The boundary of the solid medium is structured as a low-reflecting boundary. In this way, the calculation area can be considered as an infinite fluid–solid layered medium, and there is no boundary reflection echo in the received signal. In the calculation results of FEM model, the first received echo after the interface echo is intercepted as the P wave echo from the solid layer. Because of the slower speed of the S wave, the echo of the S wave traveling behind that of the P wave is omitted.

**Table 2.** Parameters of fluid–solid media.

| Medium | Material | Density (kg/m$^3$) | Velocity (m/s) (P wave) | Depth (mm) |
|---|---|---|---|---|
| First layer medium | water | 1000 | 1500 | 9 |
| Second layer medium | steel | 7850 | 5778 | – |
| Scatterer | air | 1.29 | 340 | 29 |

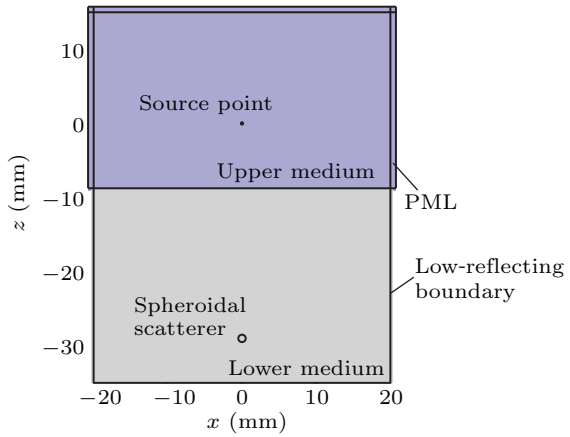



**Fig. 6.** FEM simulation model for scattering field of defects in fluid–solid media.

In Fig. 7, there are normalized echo signals of fluid–solid model at the frequencies of $f_0 = 2$ MHz and $f_0 = 3$ MHz. The results show the interface echo at $t = 12$ μs and the P wave defect echo at $t = 18.9$ μs. It can be seen from the results that the proposed method can calculate both the scattering echo of defects in fluid–fluid model and the P wave scattering echo of defects in fluid–solid model, and the results are accurate and reliable.

The computations are carried out on an Intel Core 10700 platform, with a CPU clock speed of 2.9 GHz. The CPU time for the echo computation with GFM does not exceed 30 s. While the finite element model needs to draw a grid for the whole acoustic radiation area, which takes a lot of computing time (about 30 min at $f_0 = 2$ MHz). The GFM has advantages in both calculation efficiency and precision.

The characteristic $S$ in Eq. (6) can be used to determine whether the scattering behavior is weak or strong. Scattering echoes under different $S$ conditions are shown in Fig. 8, by using the GFM and Born approximation method. It can be seen from the figure that when $S = -0.2$, the waveform of Born approximation is consistent with that of the exact solution. While if the scattering intensity becomes larger, the waveform and amplitude of the scattering echo of Born approximation deviates from those from the GFM solution, which are the accurate values of scattering echo. It can be observed that Born approximation induces an erroneous time delay in strong scattering

problem, the phenomenon of which was pointed out in infinite homogenous medium in previous research.[13] Since the acoustic properties of air hole are quite different from those of steel, the acoustic scattering field calculated by Born approximation is not reasonable. It is necessary to use the accurate solution to calculate the scattering echo of defects from the second layer medium, and GFM can solve this problem of defects with arbitrary shape at any scattering intensity.

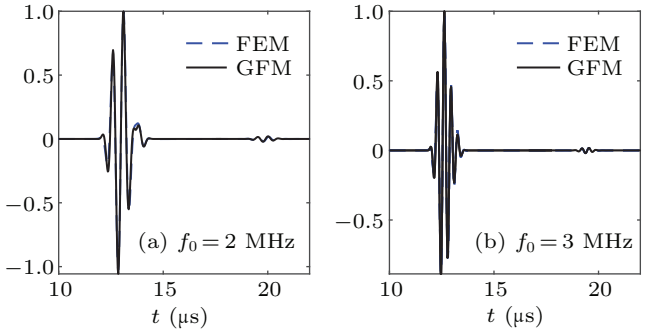



**Fig. 7.** Scattering echoes from air sphere in the second layer of fluid–solid model at different frequencies calculated by two methods: GFM (solid line) and finite element method (dashed line).

The comparison of the above results proves that the GFM has the ability to calculate the scattering ultrasounds by arbitrarily shaped, 3D rigid bodies in water-immersed steels. The basic idea of this method is equation discretization, and the application of the Green's function in two-layer fluid media. Its disadvantages are that the computational complexity and storage requirements rises dramatically as the total number of divided defect grid. Nevertheless, it is verified by plenty of tests that the calculation of GFM are faster than other existing numerical methods if the total number of defect grids is less than 3000, which is enough to be utilized to solve the scattering problem in non-destructive evaluation.

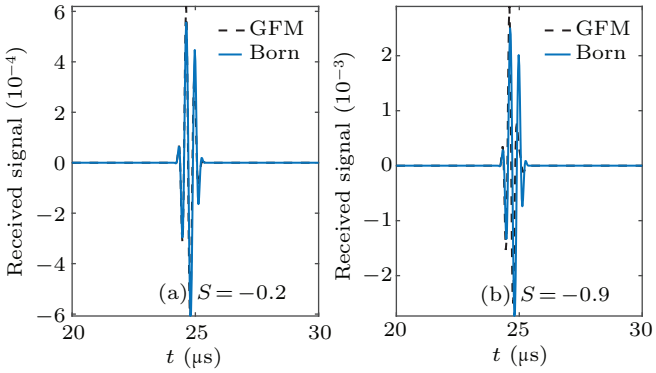



**Fig. 8.** Echoes of spherical hole with different scattering intensities in water-immersed steel calculated by Born approximation and GFM method at $S = -0.2$ (a) and $-0.9$ (b).

## 5. Characteristic analysis of scattering field of typical defects

As can be seen from the above analysis, the GFM can be used to calculate the P wave scattering echo of defects in a layered medium with high speed and accuracy. Furthermore, another advantage of GFM is that the scattering echo can be deduced according to Eq. (27) directly which does not contain the interface echo, so the characteristic analysis of the scattering field is not influenced by the interface echo.

The characteristics of the sound field scattered from defects in water immersed steel are analyzed by GFM in this section. The defect types studied are shown in Fig. 9, they being spherical hole, flat-bottom hole, through-hole, and crack defects. It is assumed that the sound source point is located in the first layer and the defect in the second layer. The center frequency of the excitation signal is set to 2 MHz.

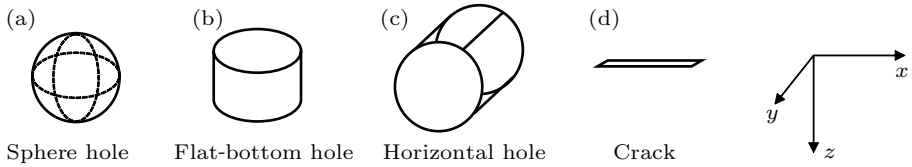



**Fig. 9.** Schematic diagrams of different types of defects.

### 5.1. Scattered field of spherical hole, flat-bottom hole, and through-hole

Acoustic parameters of the layered medium in Table 2 are selected to calculate the scattering echo. We make the vertical depth between the source point and the fluid–solid interface equal 20 mm, and that between the interface and the center of the defect equal 25 mm. The value of $R_x$ is set to zero. The radii of the sphere and cylinder are both set to 4 mm as shown in Fig. 9, and the height of the cylinder is set to 8 mm, making sizes of the two defects close to each other. The vertical cylinder in Fig. 9(b) can be regarded as a flat-bottom hole defect, and the horizontal one in Fig. 9(c) a through-hole defect.

The received defect echo signals of spherical hole and flat-bottom hole are shown in Fig. 10, where the interface echoes are not considered. Comparison between the two results in Fig. 10(a) reveals difference in echo amplitude between the two defects. This is because the scattering surface of cylinder is quite different from that of sphere. With regard to the two defect types of similar size and different shapes, the upper surface of the cylinder is plane and directly facing the backscattering receiver point, which results in very concentrated energy of the scattered sound field. While the surface of the spherical hole scatters the sound energy backward to a larger area, making the scattering echo energy dispersed and

widely distributed. In addition, it can be seen from Fig. 10(b) that the waveform durations of the signal are significantly different. The scattering echo of the spherical hole lasts longer, and the waveform changes a lot compared with the incident waveform. This is caused by the superposition of the scattered waves from different positions on the sphere, which arrive at the receiving point at different times.

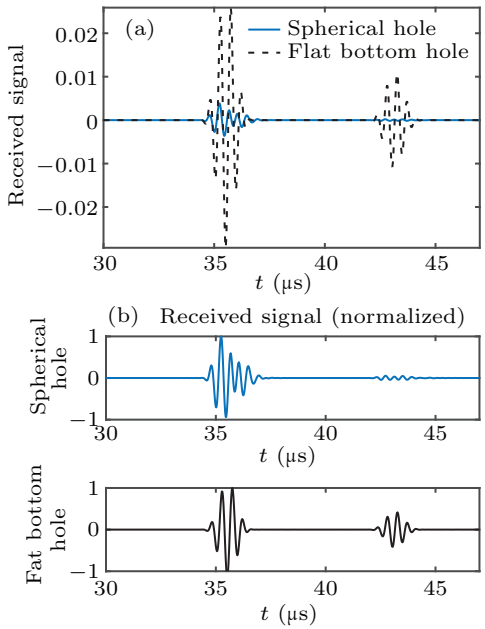



**Fig. 10.** Scattering echoes of defects in different shapes at the same position (solid line: spherical hole; dashed line: flat-bottom hole) for (a) original waveform and (b) normalized waveform.

Figure 11 shows the scattering sound fields of spherical hole and flat-bottom hole in the *xoy* plane, expressed in the unit of dB. The black curve in the figure is the contour line of the sound field dropping 3 dB down. The comparison of the results shows that the scattering sound field of the spherical hole is more widely distributed, while that of the flat-bottom hole is concentrated. This characteristic is affected by the shape of the scattering object, which can be simulated by the proposed GFM.

The results in the above analysis are for the case of $R_x = 0$, which means the source point is located right above the defect. However, the sound source may not be located right above the defect in practice. Figure 12 shows the scattering sound fields in the case of $R_x = 10$ mm, where the defect is located at the position ($x = 10$ mm, $y = 0$, $z = 45$ mm) and other parameters are the same. As can be seen from the results in the figures, the maximum position of the received scattered sound field shifts rightwards due to the oblique incident of the sound wave on the defect surface. The distribution of the scattered sound field of the spherical hole is more dispersed than that of the flat-bottom hole, and the 3 dB falling envelope of the spherical hole becomes more irregular than that of flat-bottom hole.

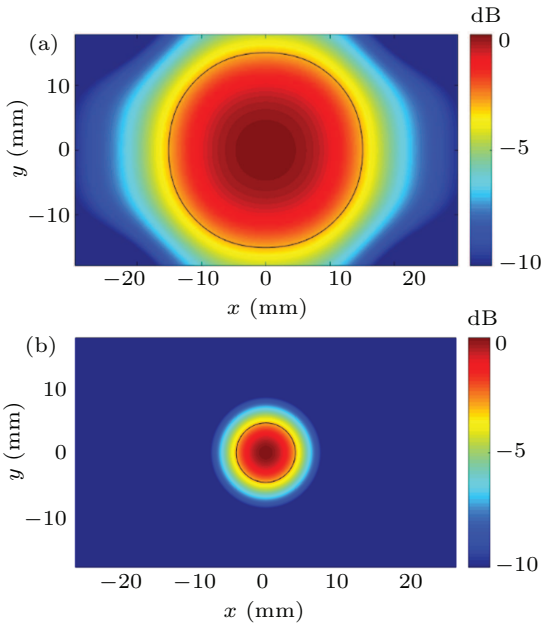



**Fig. 11.** Scattered sound fields of defects in different shapes at $R_x = 0$ for (a) spherical hole and (b) flat-bottom hole.

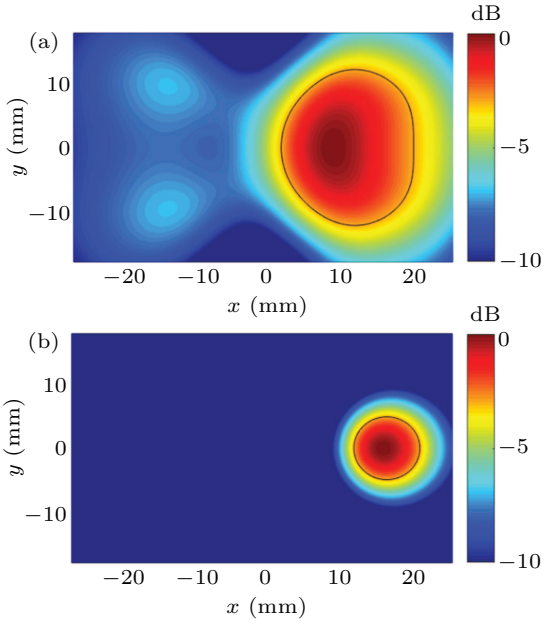



**Fig. 12.** Scattered sound fields of defects in different shapes at $R_x =$ 10 mm for (a) spherical hole and (b) flat-bottom hole.

Keeping these parameters unchanged, we set $R_x = 0$ and the radius of the flat-bottom hole $r_0 = 2$ mm and $r_0 = 5$ mm respectively. The waveform of received echo are shown in Fig. 13. Figure 13(a) shows that the two echoes have the same arriving time and extremely different pressure amplitudes, and the amplitude of the flat-bottom hole with radius $r_0 = 5$ mm is higher. Figure 13(b) indicates that the normalized echo waveforms of flat-bottom in different sizes are basically the same and the duration for the case of $r_0 = 5$ mm is slightly longer. The wavelet behind the scattering echo is a secondary scattering echo after the primary scattering echo that is reflected from the steel–water interface and reaches the flat-bottom hole. The secondary scattering echo of the flat-bottom hole with $r_0 = 5$ mm increases significantly.

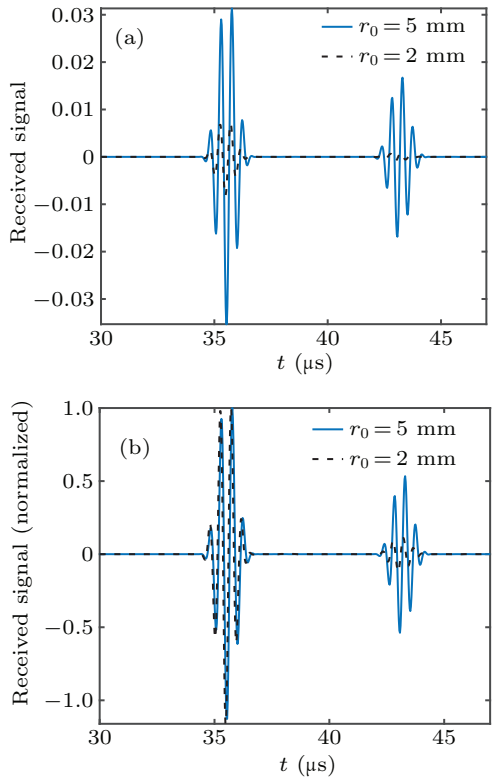



**Fig. 13.** Scattering echoes of flat-bottom holes with different sizes at the same position (solid line: $r_0 = 5$ mm; dashed line: $r_0 = 2$ mm) for (a) original waveform and (b) normalized waveform.

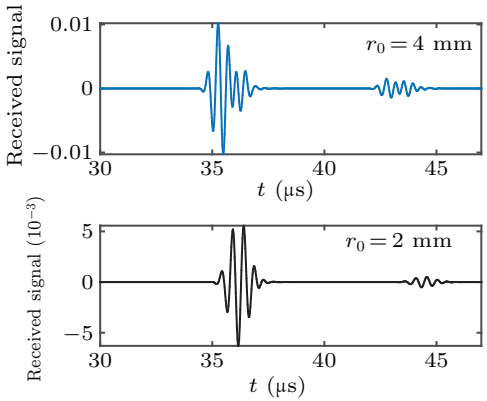



**Fig. 14.** Scattering echoes of through-holes with different sizes at the same position (blue line: $r_0 = 4$ mm; black line: $r_0 = 2$ mm)

Defect echoes of throughholes with different radii are shown in Fig. 14. The comparision among the waveforms in Fig. 14, the blue line waveform in Fig. 10(b) and the dashed line in Fig. 13(b) shows that if $r = 2$ mm, the waveform of through-hole is similar to that of flat-bottom holes. While for $r = 4$ mm, the echo waveform becomes similar to that of the spherical hole. As the through-hole radius changes from 2 mm to 4 mm, the echo amplitude increases significantly and the waveform duration becomes longer. By observing the amplitude of the blue line in Fig. 14 and received signals in Fig. 10(a), it can be seen that if the defect sizes are close to each other, the echo amplitude of through hole is larger than that of the spherical hole and smaller than that of the flat-bottom hole. This indicates that the scattering echo of the through-hole has the properties of both spherical hole and bottom hole. In the $x$ direction, there appear curved scattering and energy dispersed, meanwhile in the $y$ direction the scattering is planar and energy is concentrated.

Figure 15 shows the sound field distributions of three different types of defects in the $x$ direction, and their sizes are chosen to be similar to each other: radii equal 4 mm and heights of the cylinder equal 8 mm. The $\theta_r$ of abscissa axis indicates the angle between $oz$ axis and the line connecting receiving point and defect center. The straight line in the figure indicates the $-6$ dB dropping height of the scattered echo. Now define the 6-dB scattering angle as twice the angle when the amplitude drops to half half the maximum value. From the result it can be calculated that the 6-dB scattering angles of the three different defects are $2\pi/7$, $\pi/4$, and $\pi/9$, respectively. The attributes of the three defects are different, which leads to the magnitudes of the 6-dB scattering angles of these three kinds of defectsare in the following order: spherical hole's greater than through-hole's greater than flat-bottom hole's.

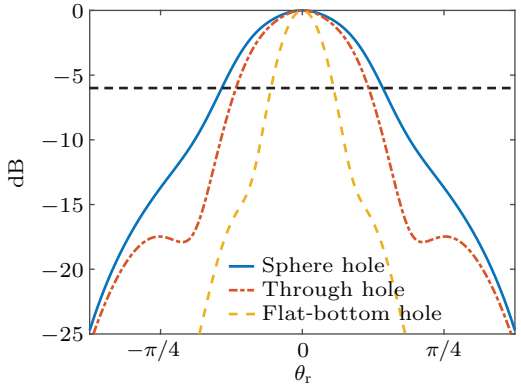



**Fig. 15.** Distributions of scattered sound fields of different types of defects on the $x$ axis (solid line: spherical hole, dashed line: transverse hole, dotted line: flat-bottom hole).

### 5.2. Scattered field of crack defect

The GFM can also calculate the scattered echo of defects in other shapes like crack defect. Now, the crack defect is assumed to be parallel to the $ox$ axis, and its length to be 14.4 mm (5 times the wave length in steel). Figure 16 shows the spatial distribution of the scattering field of crack defect. The black curve in the figure represents the contour line of the sound field dropping 3 dB down. According to the $-3$-dB envelope in the figure, the influence of defect shape on the scattering field can be seen clearly from the figure.

Keeping the position of the source point unchanged, the phenomena of acoustic wave incident on the defect from different angles are revealed by changing the crack inclination angle $\theta_d$. Figure 17(a) shows the schematic diagram of simulation model, where the components of the whole model keep still in the $y$ direction. In order to analyze the characteristics of the received scattering sound field of cracks at different angles, five inclination angles are set in equal intervals within $\pi/9$ for cracks of the same length, and the results are obtained

by simulation. The distributions of scattering sound fields on the $x$ axis of crack defects with different inclination angles are shown in Fig. 17(b).

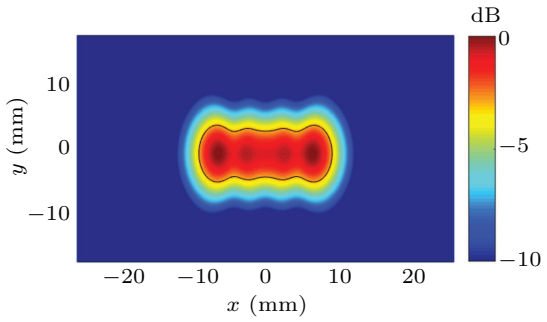



**Fig. 16.** Scattering sound field of water immersed crack defect.

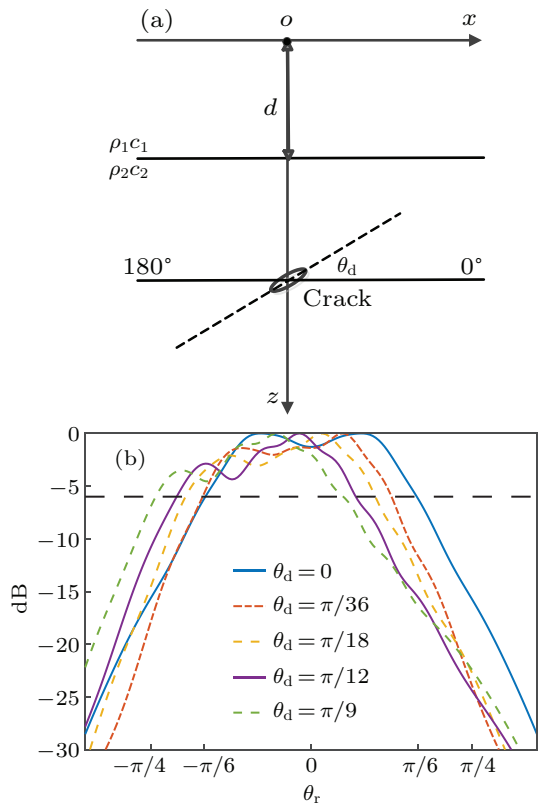



**Fig. 17.** (a) Schematic diagram of sound field simulation of crack defect and (b) distribution of scattering sound fields on the $x$ axis of crack defects with different inclination angles.

As can be seen from the curves in the figure, if $\theta_d = 0$, the crack is parallel to the $x$ axis, and the sound field distribution is symmetric in the $x$ direction. The maximum value of the scattering sound pressure is located above two ends of the crack, and the pressure amplitude right above the center of the crack decreases slightly. If the crack defect becomes inclined with a non-zero angle $\theta_d$, the maximum value of the scattering sound pressure is located above the right end of the crack. Moreover, the scattered sound field of the crack presents a distribution form: low in the left and high in the right. As $\theta_d$ increases, the peak position gradually shifts leftwards, and the amplitude at the left end gradually decreases. The −6-dB drop width changes slightly as $\theta_d$ increases. The above analyses show that the inclination angle of crack to be measured has a very significant influence on the received sound field, and the general direction of the crack located just below the probe can be judged according to the distribution of the scattered sound field.

From the above results and analyses, it can be seen that this proposed method can be used to calculate the scattered sound fields of spherical hole, through hole, flat-bottom hole, and other defects under 3D conditions, which is helpful in improving the understanding of the scattering characteristics of different defects, and developing more reasonable detection schemes for different types of defects in nondestructive testing.

## 6. Conclusions

In this work, the Green's function in two-layer fluid media is derived by using the method of stationary phase at high frequency. According to the sound wave equation and the Green's function, an efficient method of computing the precise scattering field of arbitrarily shaped scatterer in two-layer media is derived. This method can be used to calculate both weak scattering and strong scattering problem where there exists a dramatic change of acoustic impedance. The main advantage of this method is an easy numerical implementation and a good computation speed. Furthermore, it is proved that the scattering echo in fluid–solid model can also be calculated by using the Green's function presented here. Scattering fields of defects in water-immersed steel with different shapes and sizes are calculated and discussed. The proposed GFM and its result can enhance the understanding of scattering echoes from defects with different types in layered media and help improve the performance of water-immersed nondestructive test techniques.

Actually, the method proposed here may have potential applications in research of scattering field in transversely isotropic or anisotropic medium if the analytical expression of Green's function is obtained. Moreover, this method may be useful if it is combined with some ultrasonic imaging methods, for instance, the CS inverse scattering framework method proposed in Refs. [24,25]. or total focusing method proposed in Ref. [26]. This method may also be helpful in investigating the performances of ultrasonic imaging of layered media.

## Acknowledgement

Project supported by the Key Research Program of Frontier Sciences, Chinese Academy of Sciences (Grant No. ZDBS-LY-7023).

## References

[1] Zhang H, Zhang H Y, Xu M Y, Fan G P, Zhu W F and Chai X D 2019 *Chin. Phys. B* **28** 074301
[2] Dai Y X, Yan S G and Zhang B X 2020 *Chin. Phys. B* **29** 034304

[3] Shao Z H, Qiao X G, Chen F Y and Rong Q Z 2018 *Chin. Phys. B* **27** 094218
[4] Zhu Y H, Carson P L, Yuan J, Pinter S Z, Kripfgans O D, Cheng Q, Wang X D, Tao C, Liu X J and Xu G 2017 *Chin. Phys. B* **26** 064301
[5] Chu Z Q, Yuan J, Stephen Z P, Oliver D K, Wang X D, Paul L C and Liu X J 2015 *Chin. Phys. B* **24** 104303
[6] Zhang B 2007 *J. Acoust. Soc. Am* **121** 1440
[7] Bostrom A and Zhang B 2005 *IEEE Trans. Ultrason. Ferroelectr. Freq. Control* **52** 1594
[8] Guo Z C, Yan S G and Zhang B X 2019 *Chin. Phys. B* **28** 114302
[9] Banerjee S, Kundu T and Alnuaimi N A 2007 *Ultrasonics* **46** 235
[10] Banerjee S and Kundu T 2008 *J. Acoust. Soc. Am.* **123** 1371
[11] Aprameya K S, Anand R S, Mishra B K and Ahmed S 2009 *Nondestruct. Test. Eval.* **24** 289
[12] Haddadin O S and Ebbini E S 1998 *IEEE Trans. Ultrason. Ferroelectr. Freq. Control* **45** 1485
[13] Darmon M, Calmon P and Bele 2004 *Ultrasonics* **42** 237
[14] Huang R, Schmerr L W and Sedov A 2006 *Ultrasonics* **44** e981
[15] Chen Z and Zheng W 2010 *SIAM J. Numer. Anal.* **48** 2158
[16] Jiang X, Qi Y and Yuan J 2019 *Commun. Comput. Phys.* **25** 266
[17] Zampolli M, Tesei A, Canepa G and Godin O A 2008 *J. Acoust. Soc. Am.* **123** 4051
[18] Boag A, Leviatan Y and Boag A 1989 *IEEE Trans. Ultrason. Ferroelectr. Freq. Control* **36** 119
[19] Singher L, Segal Y and Shamir J 1995 *Ultrasonics* **33** 281
[20] Schmerr L W 1998 *Fundamentals of Ultrasonic Nondestructive Evaluation* (Ames, Iowa: Markys G C, Giovanni B R, Jiri T and Marijn V) p. 275
[21] Chandrasekhar B and Rao S M 2004 *J. Acoust. Soc. Am.* **115** 1926
[22] Holland K R and Fahy F J 1997 *A guide to the exploitation of vibroacoustic reciprocity in noise control technology* (Southampton: Nelson P A) p. 3
[23] Wu H, Chen J, Yang K and Hu X X 2016 *Meas. Sci. Technol.* **27** 045401
[24] Schiffner M F and Schmitz G *Proceedings of* 2011 *IEEE International Ultrasonics Symposium*, October 18–21, 2011, Orlando, USA, pp. 688–691
[25] David G, Robert J L, Zhang B and Laine A F 2015 *J. Acoust. Soc. Am.* **137** 2773
[26] Holmes C, Drinkwater B W and Wilcox P D 2005 *NDT E Int.* **38** 701